10 Analog Quantum Simulations of the Hubbard Model

Walter Hofstetter
Institute for Theoretical Physics
Goethe-University Frankfurt
Max-von-Laue-Strasse 1
D-60438 Frankfurt/Main

Contents

E. Pavarini and E. Koch (eds.)
Simulating Correlations with Computers
Modeling and Simulation Vol. 11
Forschungszentrum Jülich, 2021, ISBN 978-3-95806-529-1
http://www.cond-mat.de/events/correl21

1 Introduction

Ultracold quantum gases in optical lattices are highly tunable quantum many-body systems, which allow investigation of strongly correlated synthetic quantum matter [1,2]. They illustrate Feynman's visionary idea of a universal quantum simulator [3], and give access to (analog) quantum simulation of strongly correlated electronic systems, for example high-temperature superconductors [4,5], Mott insulators, or quantum magnets. Also bosonic quantum phases and phase transitions can be studied, for example the paradigmatic superfluid to Mott insulator (MI) transition [6]. Even more exotic types of quantum matter, such as Fermi-Hubbard models with higher internal SU(N) symmetry can be emulated using optical lattices [7,8].
Ideally, quantum simulations of the Hubbard model should address regimes or (universal) aspects of a complex and less tunable quantum system (e.g. a quantum material), which are hard to investigate on classical computers due to the exponential growth of many-body Hilbert space with increasing particle number, which limits diagonalization-based methods, and due to the (dynamical) sign problem in quantum Monte Carlo (QMC) simulations [9, 10]. Highly tunable model parameters, flexible preparation of initial states, and efficient measurement techniques are key distinguishing features of optical lattice emulators, which allow observing quantum many-body dynamics on the intrinsic length and time scales of these systems.
In these lecture notes we will focus on analog, rather than digital quantum simulation [11].

2 Optical lattice emulation of the Hubbard model

The Hubbard model [12] is the simplest microscopic lattice model of itinerant, interacting electrons in a solid. It has been successfully applied to describe, for example magnetic ordering, metal-insulator transitions and d-wave superconductivity [4,5]. For spin-½ fermions in a single band it is given by the Hamiltonian

$$\hat{H} = -t \sum_{\langle ij\rangle,\sigma} \left(\hat{c}^\dagger_{i\sigma} \hat{c}_{j\sigma} + \text{h.c.} \right) + U \sum_i \hat{n}_{i\uparrow} \hat{n}_{i\downarrow} + \sum_{i\sigma} \varepsilon_i \hat{n}_{i\sigma} \tag{1}$$

containing a kinetic energy (hopping) with matrix element t between nearest-neighbor lattice sites $\langle ij\rangle$ and a purely local (on-site) Hubbard interaction term of strength U. A schematic illustration is shown in Fig. 1. $\sigma = \uparrow, \downarrow$ labels spin, $\hat{c}^\dagger_{i\sigma}$ denotes the creation operator on lattice site i, and $\hat{n}_{i\sigma}$ is the local number operator for spin σ. We have included an additional single-particle potential ε_i, which could arise due to spatial randomness or due to an external potential, such as an optical or magnetic trap for ultracold atoms.
This simple version of the Hubbard model (1) is highly idealized. In solids, even in metals, the screening length of the Coulomb interaction can be significantly larger than the lattice constant, which leads to further terms in the Hamiltonian, for example longer-range interactions [12]. The coupling to lattice phonons can be relevant as well. In optical lattice realizations of the Hubbard model, to be discussed below, these additional terms are in general absent, but can be introduced in a controlled way, e.g., by dressing with Rydberg-excited states [13] or by coupling to dynamical phonons of trapped ion crystals [14].

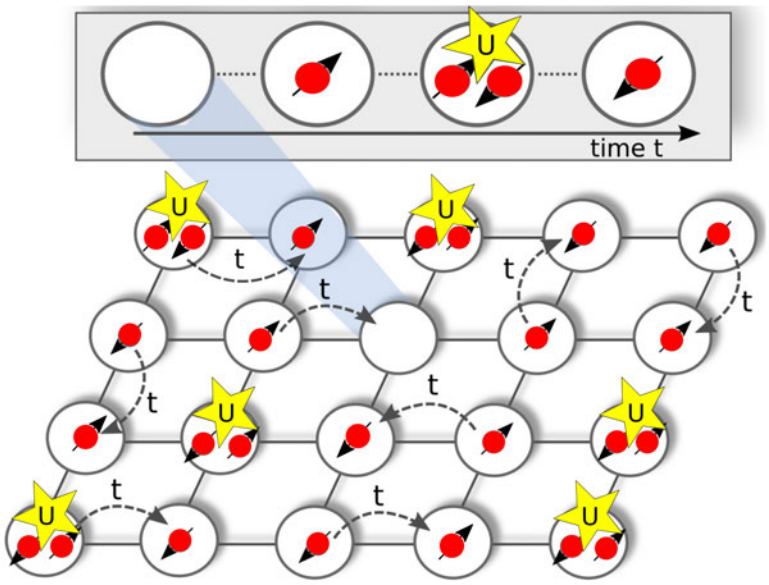

Fig. 1: *Single-band Fermi-Hubbard model on the square lattice.*
Figure reprinted from [2], ©IOP Publishing Ltd. CC BY 3.0.

(Numerically) exact solutions of the Fermi-Hubbard model exist only in one spatial dimension (Bethe Ansatz, Density-Matrix Renormalization Group (DMRG)) and in infinite dimensions (Dynamical Mean-Field Theory (DMFT)) [15]. In particular, due to basic limitations of simulation techniques (Quantum Monte-Carlo, DMRG, exact diagonalization) many questions remain open regarding the low-temperature phase diagram of the 2d Hubbard model, which is believed to be highly relevant for the description of high-temperature superconductivity [16]. On the other hand, interacting fermions [17] or bosons [18] in optical lattices provide a controlled and tunable analog quantum simulator of the pure Hubbard model. Quantum-gas microscopy techniques [19] allow single-site resolved measurements of charge and spin order, for example in (doped) Mott insulators [20–22], and give access to measurements of nonequilibrium particle and spin dynamics in real time [23–25].

Optical lattices are standing light-waves created by interfering, pairwise counterpropagating laser beams; see for example Fig. 2 (left). Neutral atoms interact with the optical lattice via the AC Stark effect, which results in an effective (time-averaged) lattice potential, see the schematic illustration in Fig. 2 (right). For a simple cubic lattice with infinite extension this potential is separable and given by

$$V_{\mathrm{lat}}(x,y,z) = V_0 \left(\sin^2(kx) + \sin^2(ky) + \sin^2(kz)\right) \tag{2}$$

where $k = 2\pi/\lambda$ is the wavenumber of the lattice-lasers. The lattice amplitude V_0 depends on the atomic polarizability and the intensity of the light [26], and is positive (negative) for blue (red) detuning of the lasers. The characteristic energy scale is set by the recoil energy $E_r = \hbar^2 k^2/2m$, with typical values of order $O(\mathrm{kHz})$. Many different lattice geometries have been realized in this way, including triangular [27], Kagome [28], and artificial graphene [29].

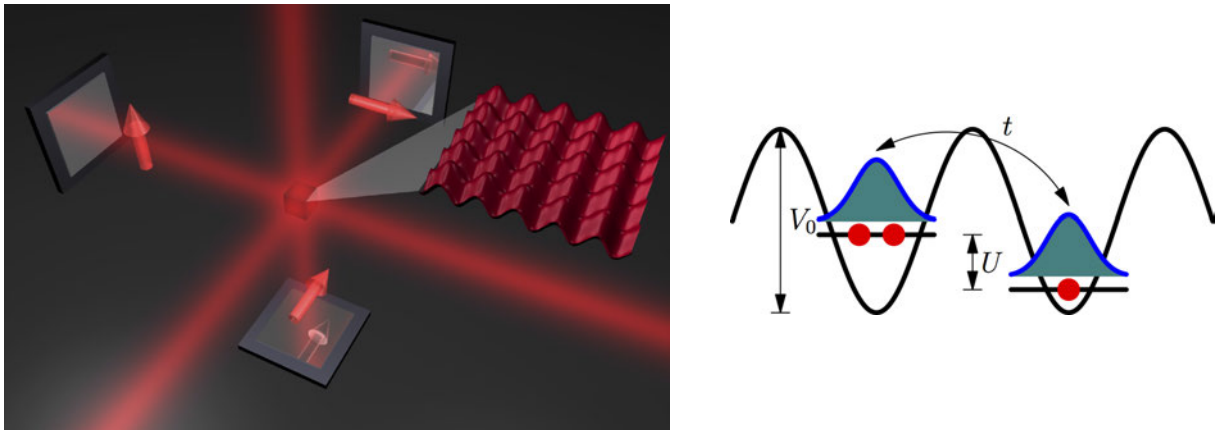

Fig. 2: *Left: Cubic optical lattice. For illustration purposes, a 2d slice is shown. The three lattice lasers have mutually orthogonal polarizations indicated by the arrows, and are each retroreflected from a mirror. Figure reprinted from [30] with permission. Right: Schematic illustration of spinless bosons in an optical lattice with hopping t and on-site Hubbard interaction U. Figure reprinted from [2], ©IOP Publishing Ltd. CC BY 3.0.*

Compared to solid-state crystals, the lattice constant of an optical lattice is much larger ($a = O(100\,\mathrm{nm})$ instead of $O(\text{Å})$), and the resulting energy-scales are much lower (kHz instead of eV). This results in much slower quantum dynamics than in electronic solids, which has made it possible to observe in-situ the quantum phases and nonequilibrium dynamics of ultracold atoms on their intrinsic time-scales with single-site, single-atom resolution, via quantum-gas microscopy [19].

Ultracold gases in optical lattices are almost ideal closed quantum systems, highly isolated from their environment, with the residual dissipation mostly arising from spontaneous emission [26], which leads to heating that typically starts to dominate after times of several 100 ms. Note that optical lattices are very clean, i.e., free of defects, but they are intrinsically finite (typical lengths of $O(100)$ lattice sites) and typically inhomogeneous due to the profile of the Gaussian laser beams, although quasi-flat "box potentials" can also be engineered. This confinement-induced inhomogeneity can often be well described within a local density approximation, where each lattice site i is treated as part of an infinite homogeneous system with an effective chemical potential $\mu_i = \mu - \varepsilon_i$ that depends on the lattice site.

Let us now show that the low-energy effective Hamiltonian of an ensemble of ultracold atoms in an optical lattice is given – under suitable conditions – by the single-band Hubbard model. We consider, for the moment, a homogeneous lattice without external confinement potential. According to Bloch's theorem, the single-particle eigenstates in an optical lattice can be written as

$$\phi_{\boldsymbol{q}}^{(\alpha)}(\boldsymbol{r}) = e^{i\boldsymbol{q}\cdot\boldsymbol{r}}\, u_{\boldsymbol{q}}^{(\alpha)}(\boldsymbol{r}). \tag{3}$$

The index α labels different bands, and $\boldsymbol{q} = (q_x, q_y, q_z)$ is the quasimomentum. On a simple cubic lattice its components are in the range $q_{x,y,z} \in (-\pi/a, \pi/a]$, with the lattice constant $a = \lambda/2$ determined by the laser wavelength. $u_{\boldsymbol{q}}^{(\alpha)}(\boldsymbol{r})$ is a lattice-periodic function.

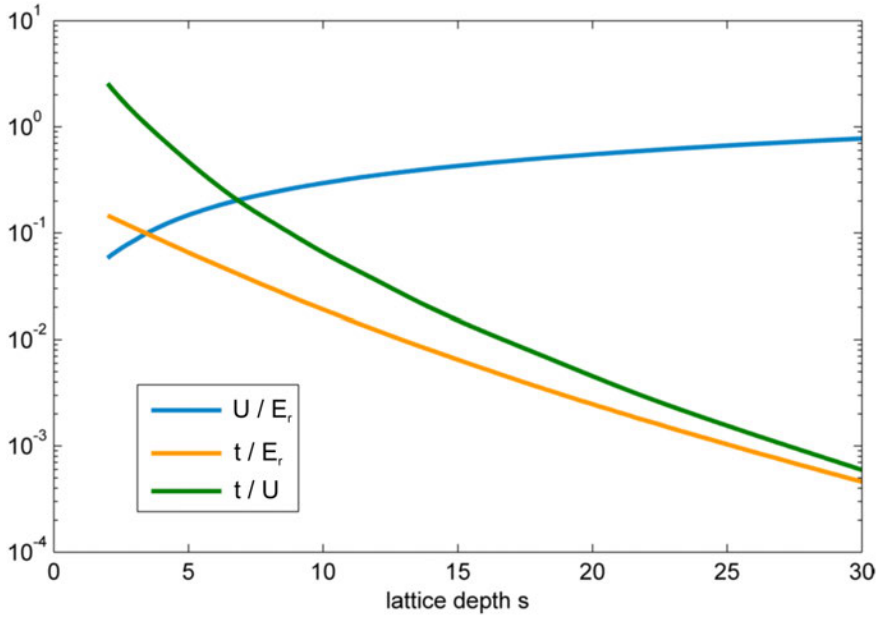

Fig. 3: *Hubbard parameters t and U and their ratio, shown here as a function of the dimensionless lattice depth s for ^{87}Rb in a 812 nm optical lattice. Both the hopping t and the ratio t/U decay approximately exponentially for deep lattices. Figure adapted from [30] with permission.*

To formulate a tight-binding Hamiltonian we use Wannier functions, which also form an orthonormal single-particle basis and are maximally localized at the respective lattice sites. They are related to the Bloch functions by

$$w^{(\alpha)}(\boldsymbol{r}-\boldsymbol{r}_i) = N^{-1/2} \sum_{\boldsymbol{q}} e^{-i\boldsymbol{q}\cdot\boldsymbol{r}_i}\, \phi_{\boldsymbol{q}}^{(\alpha)}(\boldsymbol{r}) \tag{4}$$

with $\boldsymbol{r}_i$ the position of the i-th lattice site and N the total number of sites. Note that computing the maximally localized Wannier functions usually involves numerical optimization of the phases of the Bloch states. An efficient alternative is calculating Wannier functions as eigenfunctions of the band-projected position operator [29, 30], which can also be done for systems with broken lattice translational invariance, for example due to disorder.

If the filling (the number of particles per site), the temperature T, and the Hubbard interaction strength U are low enough, it is sufficient to consider only the lowest Bloch band with $\alpha = 1$. This will be assumed in the following discussion, where the band index will be omitted. We write the kinetic energy as $\hat{H}_{\rm kin} = -t \sum_{\langle ij\rangle,\sigma} \hat{c}^\dagger_{i\sigma}\hat{c}_{j\sigma} + \text{h.c.}$, where $\hat{c}^\dagger_{i\sigma} = \int d^3r\, w(\boldsymbol{r}-\boldsymbol{r}_i)\, \hat{\Psi}^\dagger_\sigma(\boldsymbol{r})$ creates a particle with mass m and internal (hyperfine) state σ in the lowest Wannier state on site i. The resulting tunneling matrix element between neighboring sites i and j is given by $t = -\int d^3r\, w^*(\boldsymbol{r}-\boldsymbol{r}_i)\left(-\hbar^2\boldsymbol{\nabla}^2/2m + V_{\rm lat}(\boldsymbol{r})\right) w(\boldsymbol{r}-\boldsymbol{r}_j)$. For sufficiently deep optical lattices with a dimensionless depth $s \equiv V_0/E_r \gg 1$, tunneling beyond nearest neighbors $\langle ij\rangle$ can in most cases be neglected. If the lattice is also separable, one obtains approximately $t = (4/\sqrt{\pi}) E_r\, s^{3/4} \exp\left(-2s^{1/2}\right)$ [1].

Two-particle interactions between ultracold neutral atoms are usually dominated by s-wave scattering and can be described by a contact interaction [1]

$$\hat{H}_{\rm int} = g \int d^3r \; \hat{\Psi}^\dagger_\uparrow(\boldsymbol{r})\hat{\Psi}^\dagger_\downarrow(\boldsymbol{r})\hat{\Psi}_\downarrow(\boldsymbol{r})\hat{\Psi}_\uparrow(\boldsymbol{r})$$

of strength $g = 4\pi\hbar^2 a_s/m$ (where a_s is the scattering length), which has been written here for fermions with two hyperfine ("spin") states $\uparrow, \downarrow$. For a sufficiently deep optical lattice with $s \gg 1$ and in the absence of Feshbach resonances we can again use the single-band approximation. The dominant interaction term is then given by $\hat{H}_{int} = U \sum_i \hat{n}_{i\uparrow}\hat{n}_{i\downarrow}$ with the Hubbard interaction parameter $U = g \int d^3r \, |w(\boldsymbol{r})|^4 \approx \sqrt{8/\pi}(2\pi a_s/\lambda)s^{3/4}E_r$. We have thus obtained the single-band Fermi-Hubbard model as given in Eq. (1) [17]. The additional onsite energy ε_i describes the confinement potential, or additional optical potentials (e.g. superlattices or spatially fluctuating optical Speckle potentials) which may be superimposed onto the primary optical lattice. Experimentally the correlation strength U/t is highly tunable from values $U/t \approx 0$ to $|U|/t > 1000$, either by varying the optical lattice depth as shown in Fig. 3, or by using Feshbach resonances [1] to change a_s.

The bosonic Hubbard model [31]

$$\hat{H} = -t \sum_{\langle ij \rangle} \left(\hat{b}^\dagger_i \hat{b}_j + \text{h.c.} \right) + \frac{U}{2} \sum_i \hat{n}_i(\hat{n}_i - 1) + \sum_i \varepsilon_i \hat{n}_i \tag{5}$$

can analogously be derived for ultracold bosons [18], and has been first implemented in a pioneering experiment exploring the superfluid – MI transition [6].

Corrections to the standard single-band Hubbard models (1) and (5) become important for strong contact interactions, for example close to Feshbach resonances or in shallow lattices. A density dependence of the Hubbard interaction parameter U has been measured [32]. It can be described, together with other corrections such as density-dependent hopping, pair tunneling, and next-neighbor interactions, by including contributions of higher Bloch bands in an effective single-band model [33]. Independently, it is also possible to populate higher bands of an optical lattice and to study multi-band phenomena.

Let us now give a brief overview of techniques for measuring observables (e.g. particle- or spin-density excitation spectra) in cold atom quantum simulators. Time-of-flight (TOF) spectroscopy is performed by ballistic expansion of the atomic cloud in the absence of interactions, followed by measurement of the density via absorption imaging. It allows to extract the in-trap momentum distribution of the initial many-body state as $\langle \hat{n}(\boldsymbol{r}) \rangle_{\rm TOF} \propto \langle \hat{n}(\boldsymbol{k}) \rangle_{\rm trap}$ where $\boldsymbol{k} = m\boldsymbol{r}/\hbar t$ [1]. Using a slow initial ramp-down of the optical lattice that is adiabatic with respect to the band gap, one can also directly image the Bloch quasimomentum distribution, including higher Brillouin zones [34]. Moreover, spatial correlations of the noise in single-shot TOF images can be used to infer momentum correlations in the initial many-body state, and thus to detect for example MI states or magnetic long-range order [35, 36].

Interaction effects can be studied by radio-frequency (RF) spectroscopy [37], where the atoms initially in the hyperfine state $|g\rangle$ are excited to state $|e\rangle$ by an applied RF field, and the fraction of excited atoms is then detected. This has allowed, for example, to measure the pairing

gap in a strongly interacting superfluid Fermi gas [38], similar to tunneling experiments in superconductors. Using a momentum-resolved version of RF spectroscopy [39] the fermionic spectral function $A(\boldsymbol{k},\,\omega) = -\frac{1}{\pi}\mathrm{Im}\,G^R(\boldsymbol{k},\,\omega)$ at frequency ω and momentum $\boldsymbol{k}$ has been measured experimentally, where $G^R(\boldsymbol{k},t) = -i\Theta(t)\,\langle\Psi_0|\{\hat{c}_{\boldsymbol{k}}(t),\hat{c}^\dagger_{\boldsymbol{k}}(0)\}|\Psi_0\rangle$. This is an analog of angle-resolved photoemission spectroscopy (ARPES) in solids.

Two-photon Bragg spectroscopy allows probing dynamical correlation functions such as the dynamical structure factor $S(\boldsymbol{k},\,\omega) \propto \sum_f \left|\langle f|\hat{\rho}^\dagger(\boldsymbol{k})|g\rangle\right|^2 \delta\big(\hbar\omega - (E_f - E_g)\big)$ given here at zero temperature. $\hat{\rho}(\boldsymbol{k})$ is the Fourier transform of the density, and $|f(g)\rangle$ the initial (final) state of the many-body system. This is achieved by a two-photon transition, where atoms absorb a photon from one laser and emit a photon into a second laser mode, which leads to a momentum and energy "kick" $\hbar\boldsymbol{k}_{\mathrm{Bragg}} = \hbar(\boldsymbol{k}_1 - \boldsymbol{k}_2)$ and $\hbar\delta = \hbar(\omega_1 - \omega_2)$, where $\hbar\boldsymbol{k}_i$ and $\hbar\omega_i$ with $i = 1, 2$ denote the momenta and energies of the two lasers. Bragg scattering has also been applied in the strongly correlated regime and beyond linear response, where the amplitude mode of strongly interacting bosons in a cubic lattice has been observed [40]. A related approach is lattice amplitude modulation spectroscopy, which has been applied, for example, to identify the Mott-insulator phase of fermions in a cubic optical lattice [41].

Optical quantum-gas microscopy, first realized for bosonic ^{87}Rb [19], has revolutionized quantum simulators based on ultracold atoms. Fluorescence photons created by in-trap laser cooling are detected with a high-resolution imaging objective, which allows imaging of single atoms on individual sites of an optical lattice. This technique also allows local control and manipulation, for example performing spin-flips of individual atoms [42]. It is also applicable to fermionic quantum gases, where it has for example been applied to image the fermionic Mott insulator [43], including the "wedding cake structure" of the density profile corresponding to spatial domains of different phases (Fermi liquid, band- and Mott-insulator).

3 Mott insulator transition

Mott insulators and the associated metal-insulator transitions are of fundamental relevance in strongly correlated electronic systems, for example in transition metal oxides and organic conductors, and – with additional doping – in cuprate high-temperature superconductors [4].

Ultracold gases in optical lattices have allowed for a highly controlled experimental realization of the Mott transition, both fermionic and bosonic, which clearly separates the itinerant degrees of freedom from other effects such as phonons and defects, and which is more easily tunable than solid-state realizations. In particular, the correlation strength (the ratio U/t of Hubbard interaction and hopping) can be tuned all the way from the limit of a noninteracting Fermi gas in a lattice [34], to the "atomic limit", i.e., the deep Mott-insulator regime, where tunneling can be considered a small perturbation.

On the other hand, the theoretical description of Mott transitions has made strong progress due to advances in numerical techniques such as DMRG, QMC and, in higher spatial dimensions, DMFT [15] and its real-space generalization to inhomogeneous systems [44]. DMFT is based on a mapping of each lattice site of the Hubbard model to an (Anderson-) quantum impurity

model with the same effective local action

$$S_{\rm eff}^{(i)} = -\iint d\tau d\tau' \sum_\sigma c_{i\sigma}^\dagger(\tau)\, \mathcal{G}_0^{(i)}(\sigma,\tau-\tau')^{-1}\, c_{i\sigma}(\tau') - U\int d\tau\, n_{i\uparrow}(\tau) n_{i\downarrow}(\tau) \qquad (6)$$

that is determined self-consistently. This yields a non-perturbative description of local quantum dynamics in the original correlated lattice problem. The DMFT self-consistency loop is formed by the local Dyson equation $\mathcal{G}_0^{(i)}(\sigma,i\omega_n)^{-1} = G^{(i)}(\sigma,i\omega_n)^{-1} + \Sigma^{(i)}(\sigma,i\omega_n)$ and the lattice Dyson equation $\boldsymbol{G}(\sigma,i\omega_n)^{-1} = \boldsymbol{G}_0(\sigma,i\omega_n)^{-1} - \boldsymbol{\Sigma}(\sigma,i\omega_n)$, complemented by the requirement that the interacting local (impurity) Green's function is equal to the respective diagonal element of the full lattice Green's function: $G^{(i)}(\sigma,i\omega_n) = G_{ii}(\sigma,i\omega_n)$. Above, boldface objects are matrices with entries labeled by two lattice site indices. Calculating the self-energy $\Sigma^{(i)}$ from the local action (6) is a computationally demanding task which is performed by a quantum impurity solver, e.g., exact diagonalization, the Numerical Renormalization Group (NRG), or continuous-time Quantum Monte-Carlo (CT-QMC) [15, 45]. The full real-space extension of DMFT [44] allows simulation of inhomogeneous, correlated fermionic and bosonic lattice gases for experimentally relevant system sizes [46], even in situations where other simulation methods are not applicable. DMFT has been very successful in describing the Mott metal-insulator transition, see for example the DMFT phase diagram of the single-band Fermi-Hubbard model at half filling in Fig. 4. In particular, it has provided theoretical understanding of the narrow quasiparticle resonance in the spectral function of the correlated metallic phase close to the transition [47]. On bipartite lattices (e.g. cubic) at half filling, antiferromagnetism emerges at low temperatures for any value of the Hubbard interaction, and typically hides the paramagnetic Mott transition. On generic lattices with frustration the antiferromagnetic phase is reduced and the Mott transition can be recovered to some extent, see Fig. 4.

A Mott transition also occurs in the Bose-Hubbard model at integer filling, in this case between superfluid and Mott insulator [31]. It is captured qualitatively by a static (Gutzwiller) mean-field theory, based on a variational wavefunction that is a product over all lattice sites and connects two limiting cases: At vanishing hopping, the Mott insulator wavefunction for integer filling n can be written as $|\Psi_{\rm Mott}\rangle \propto \prod_{i=1}^N \left(\hat b_i^\dagger\right)^n |0\rangle$, while in the noninteracting case ($U{=}0$) and for arbitrary filling n the condensate can be written as a product of coherent states at the individual lattice sites: $|\Psi_{\rm cond}\rangle \propto \left(\sum_{i=1}^N \hat b_i^\dagger\right)^{nN}|0\rangle \propto \prod_{i=1}^N \exp\left(\sqrt{n}\,\hat b_i^\dagger\right)|0\rangle_i$. The development of bosonic DMFT [48] has improved theoretical understanding of the bosonic Mott insulator, capturing particle-hole excitations which lead to short-range coherence, as well as superexchange interactions in multi-component systems. Independently, large-scale QMC simulations of bosonic lattice models became feasible using the Worm algorithm [49].

The Bose-Hubbard model has been realized experimentally [6], following the proposal [18], using ^{87}Rb on a cubic optical lattice. The superfluid-Mott insulator quantum phase transition has been observed in measurements of the momentum distribution and the excitation spectrum, at a correlation strength $U/t = 5.8\,z$, with the lattice coordination number $z = 2d$, which agrees reasonably well with the static mean-field prediction. Later, a *validation* of this quantum simulator for the model (5) has been performed by finite-temperature measurements of the momentum

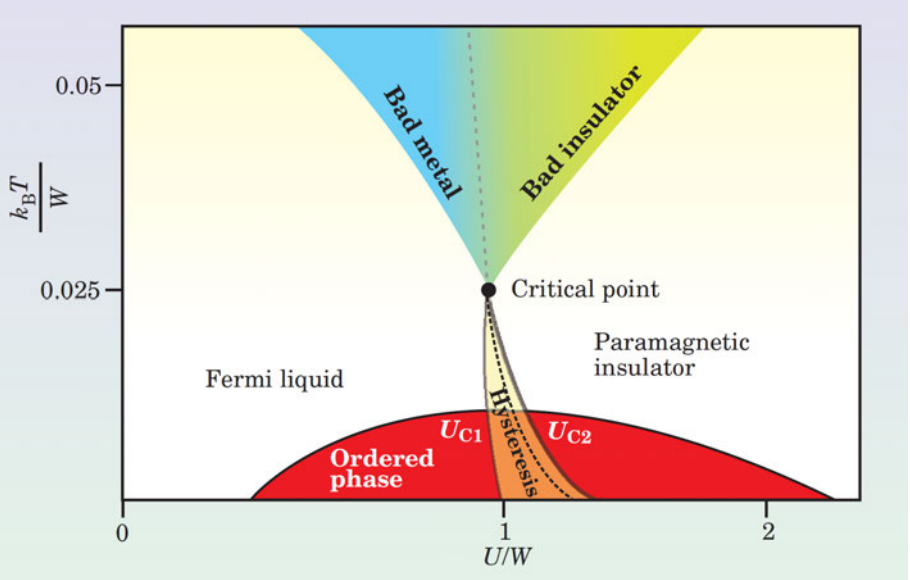

Fig. 4: *Schematic DMFT phase diagram of the homogeneous Fermi-Hubbard model (1) at half filling on a generic 3d lattice with bandwidth W. At low temperatures long-range order emerges (indicated in red), for example antiferromagnetism, depending on the lattice structure. In the orange region metallic and Mott-insulating phases coexist. At the dashed line a first-order transition occurs, which ends in a second-order critical point. At higher temperatures the Mott metal-insulator transition becomes a crossover. Figure reproduced from [47], with the permission of the American Institute of Physics.*

distribution and comparison to QMC calculations [50], which allowed determining the finite-temperature phase diagram. More recently, optical quantum-gas microscopy has given access to in-situ imaging and control with single-atom, single-site resolution [19], opening up new possibilities for optical lattice quantum simulators. It allows, for example, to image superfluid and Mott insulating domains, and to determine temperature and entropy directly from the local particle-number statistics.

The fermionic Mott transition has also been observed in ultracold gases. In [51] this was achieved by measuring the size and compressibility of the fermionic ^{40}K cloud as a function of the confinement potential, and by comparison to DMFT simulations. On the other hand, in [41] the double occupancy and particle-hole excitation energies have been determined. The crossover from the "metallic" to the Mott insulating regime was also studied for spinful ultracold fermions in artificial graphene [29]. The fermionic Mott insulator has also been imaged with quantum-gas microscopy [43], which has allowed to determine from the local particle number statistics the entropy per site, which was found to be $s_i \approx k_B \ln 2$, in agreement with theoretical expectations.

Mott insulators with larger spin $S > 1/2$ or higher symmetry groups such as SU(N) can also be implemented in optical lattices, using multiple hyperfine states. For example, an SU(6) Mott insulator of ^{173}Yb has been realized [52], with an increased spin entropy per site $s = k_B \ln N$ due to the larger number of internal states.

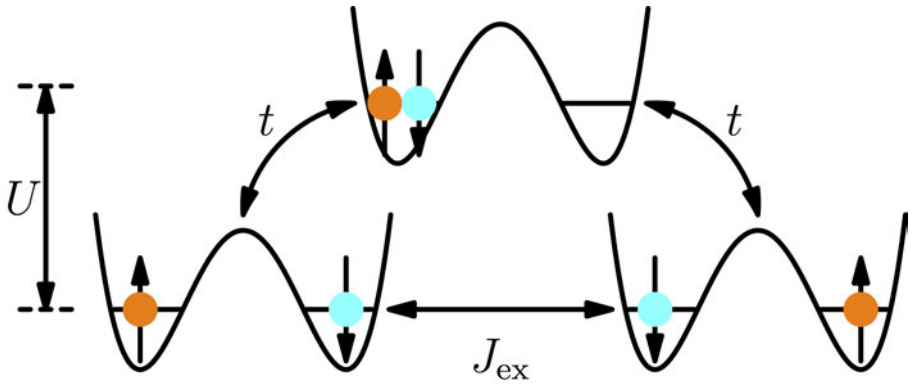

Fig. 5: *Superexchange couplings due to virtual second-order tunneling. Figure reprinted from [2], ©IOP Publishing Ltd. CC BY 3.0.*

4 Quantum magnetic correlations

For spin-½ fermions and in the "atomic" limit of vanishing tunneling $t \to 0$ the paramagnetic spin-½ Mott insulator discussed above has an extensive residual entropy $S = Nk_B \ln 2$ due to spin fluctuations. At finite t, magnetic superexchange couplings, illustrated in Fig. 5, will induce spin-spin correlations and possibly long-range magnetic order, depending on temperature.
Quantum magnetism, although studied for a long time, still poses intriguing open questions, for example whether quantum spin liquids on frustrated lattices exist, and what their properties are. In many cases it is challenging to investigate quantum magnetic correlations by numerically exact techniques, due to the sign problem (QMC), system size (exact diagonalization), or spatial dimensionality (DMRG). The same holds true for simulations of real-time nonequilibrium spin dynamics in Hubbard-type models.
Optical-lattice quantum simulators are well suited for investigating quantum spin systems. On the one hand this is due to the high tunability of lattice geometry, dimensionality and (effective) exchange couplings. On the other hand, novel observation techniques such as quantum-gas microscopy allow to measure spin ordering, magnetic correlations, and nonequilibrium spin dynamics with single-site resolution and in real-time [19].
Let us consider a two-component version of the Hubbard model for ultracold atoms [53]

$$\hat{H} = -\sum_{\langle ij\rangle\sigma}\left(t_\sigma \hat{a}^\dagger_{i\sigma}\hat{a}_{j\sigma} + \text{h.c.}\right) + U_{\uparrow\downarrow}\sum_i \hat{n}_{i\uparrow}\hat{n}_{i\downarrow} + \frac{1}{2}\sum_{i,\sigma} U_\sigma\, \hat{n}_{i\sigma}(\hat{n}_{i\sigma}-1), \tag{7}$$

where $\sigma = \uparrow, \downarrow$ is a pseudospin index, labeling either different hyperfine states or atomic species. All interactions are repulsive $U_{\uparrow\downarrow}, U_\sigma \geq 0$. This model is applicable both for bosonic and for fermionic atoms, created by $\hat{a}^\dagger_{i\sigma}$. For fermions, it is equivalent to the standard spin-½ Fermi Hubbard model, and the repulsion U_σ between equal species should then be set to infinity in the equations below. The hopping amplitudes t_σ are tunable and can be spin-dependent, e.g., due to a mass imbalance of the two species $\sigma = \uparrow, \downarrow$ [54] or spin-dependent optical lattices. Changing the s-wave scattering lengths $a_{\sigma\sigma'}$, e.g., via Feshbach resonances, allows tuning of the interactions $U_{\sigma\sigma'}$.

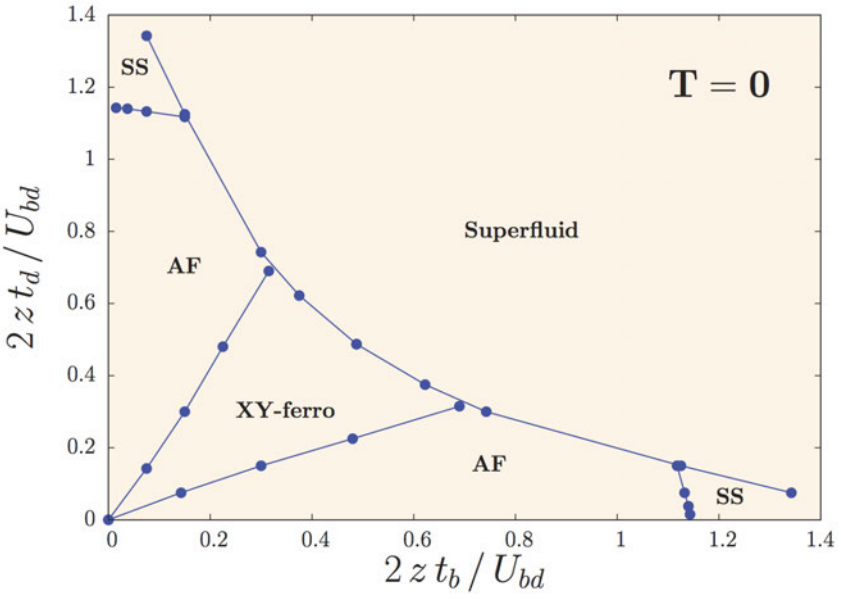

Fig. 6: *Tunable ground-state magnetic order of two-component bosons in a cubic, spin-dependent lattice, obtained by bosonic DMFT. xy-ferromagnetic, z-Néel antiferromagnetic (AF) and supersolid (SS) phases are found, in addition to the homogeneous superfluid. Here $t_{b(d)}$ corresponds to $t_{\uparrow(\downarrow)}$ in Eq. (7), $U_{b(d)}$ corresponds to $U_{\uparrow(\downarrow)}$, and U_{bd} corresponds to $U_{\uparrow\downarrow}$. Ratios between the different interactions have been fixed as $U_b = U_d = 12U_{bd}$. The total filling per site is one, with $n_b = n_d = 0.5$. Reprinted figure with permission from [55]. Copyright 2011 by the American Physical Society.*

In the Mott insulator for total filling $n_{i\uparrow} + n_{i\downarrow} = 1$ per site, and to leading order in $t_\sigma/U_{\uparrow\downarrow}$ and t_σ/U_σ the low-energy effective Hamiltonian

$$\hat{H} = \sum_{\langle ij \rangle} J_z \hat{\sigma}_i^z \hat{\sigma}_j^z \pm J_\perp (\hat{\sigma}_i^x \hat{\sigma}_j^x + \hat{\sigma}_i^y \hat{\sigma}_j^y) \tag{8}$$

is an XXZ spin model [53], with the sign $+(-)$ for fermions (bosons), and with longitudinal and transverse superexchange couplings given by

$$J_z = \frac{t_\uparrow^2 + t_\downarrow^2}{2U_{\uparrow\downarrow}} - \frac{t_\uparrow^2}{U_\uparrow} - \frac{t_\downarrow^2}{U_\downarrow} \qquad \text{and} \quad J_\perp = \frac{t_\uparrow\, t_\downarrow}{U_{\uparrow\downarrow}}\,. \tag{9}$$

For fermions these couplings are always antiferromagnetic ($t_\sigma \geq 0$ is assumed). However, for bosons, the sign of J_z can be tuned,leading, in a spin-dependent cubic lattice at unit filling, to a quantum phase transition between xy-ferromagnetism and z-Néel antiferromagnetism [53, 55], see Fig. 6. Finite-temperature DMFT calculations for the same model [56] have, in addition, found a Pomeranchuk effect, where heating the system leads to a transition from the superfluid phase to a paramagnetic Mott insulator and, as a result, non-monotonic behavior of the local particle number variance $(\Delta n_i)^2 = \left\langle \left(\hat{n}_i - \langle \hat{n}_i \rangle\right)^2 \right\rangle$, which should be observable by quantum-gas microscopy.

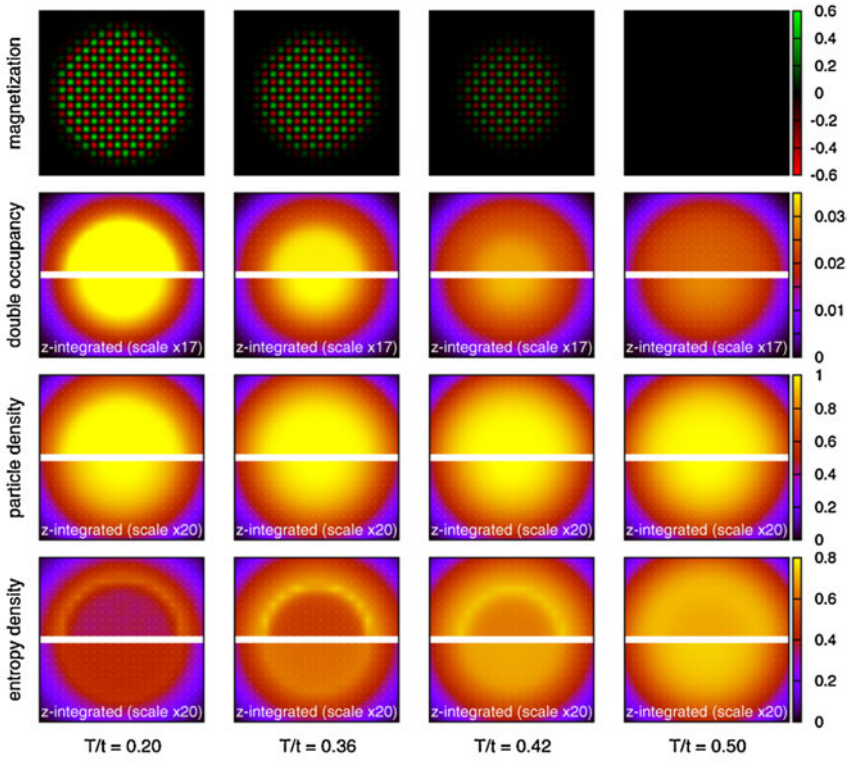

Fig. 7: *Real-space DMFT simulation of a Fermi-Hubbard model in a harmonic trap. Shown are antiferromagnetic order (first row), double occupancy D (second row), particle (3rd row) and entropy (4th row) densities per site, in the central plane of the Fermi-Hubbard model (1) on a cubic lattice with $U = 12t$ and a harmonic trapping potential $\varepsilon_i = V_0 \mathbf{r}_i^2/a^2$ with $V_0 = 0.05t$. At low temperature (left column) a large antiferromagnetic core is visible; with increasing temperature the AF order decays. In the 2nd, 3rd and 4th row the top half displays the respective observables in the central plane of the lattice, and the bottom half the corresponding values after integration along the z-axis. Reprinted figure with permission from [46]. Copyright 2010 by the American Physical Society.*

The formation of antiferromagnetic (AF) order of spin-½ ultracold fermions in a half-filled optical lattice was first proposed in [17]. It was later studied by cluster DMFT [57], which provided an estimate $s_{\text{Néel}} \approx 0.42\, k_B$ for the critical entropy per particle. Experiments with 3d optical lattices have yielded higher values $s \approx 0.77\, k_B$ in the Mott core [58], indicating that in these measurements the AF ordered regime has not yet been reached. Magnetization and entropy profiles for realistic system sizes in a harmonic trap have been obtained by real-space DMFT [46], see Fig. 7, and an enhanced double occupancy $D = \langle \hat{n}_{i\uparrow} \hat{n}_{i\downarrow} \rangle$ was found in the Néel-ordered phase.

Ultracold atoms also allow realizing multi-flavor mixtures with more than two hyperfine states and higher internal symmetry groups. This has for example been achieved with ^{173}Yb, a fermionic alkaline-earth-like element, which has been cooled into an SU(6) Mott-insulating state [52]. DMFT studies of three-component fermionic mixtures in optical lattices have predicted exotic spin and density order [59]. Note that due to enhanced Pomeranchuk cooling, adiabatic lattice loading of fermions with multiple flavors can achieve lower temperatures than for spin-½ systems [60].

Experimentally, tunable superexchange interactions in ultracold atoms, as given in Eq. (9) and shown in Fig. 5, were first seen in the spin dynamics of a mixture of two hyperfine states of ^{87}Rb in a superlattice [61]. Achieving sufficiently low entropies and temperatures of quantum gases in an optical lattice in order to observe superexchange-induced magnetic order is an experimental challenge [62], although much progress has been made. Adiabatic spin gradient demagnetization has allowed to cool a mixture of two hyperfine states of bosonic ^{87}Rb in a cubic lattice to temperatures as low as 350 pK [63]. Real-space bosonic DMFT calculations for this experimental setup have provided quantitative modeling of these results [56] and predicted that long-range magnetic order can indeed be reached by adiabatic demagnetization.

Early measurements of spin-spin correlations included a detection scheme for singlets and triplets based on merging pairs of lattice sites, which allowed to observe short-range AF correlations in dimerized and simple cubic lattices [64]. Another powerful approach is given by spin-sensitive Bragg scattering, which yields the spin structure factor

$$S^z_{\boldsymbol{q}} = \frac{1}{N}\sum_{i,j} e^{i\boldsymbol{q}\cdot(\boldsymbol{r}_i-\boldsymbol{r}_j)}\langle\hat{\sigma}^z_i\hat{\sigma}^z_j\rangle$$

and is analogous to neutron scattering in solid-state physics. In the experiment [58] a strong enhancement of $S^z_{\boldsymbol{q}}$ at the wavevector $\boldsymbol{q} = (\pi/a)(-1,-1,1)$ was observed for fermionic ^{6}Li in a cubic optical lattice, indicating Néel-type spin-spin correlations. Comparison to numerical simulations (QMC and linked-cluster expansion) allowed to estimate the temperature in this setup as 1.4-times the critical temperature of long-range AF order.

More recently, optical quantum-gas microscopy has allowed to detect spin-spin- and density-density-correlations in-situ. The spin-spin correlator $C_{\boldsymbol{d}} \propto \sum_{\boldsymbol{r}}\langle\hat{\sigma}^z_{\boldsymbol{r}}\hat{\sigma}^z_{\boldsymbol{r}+\boldsymbol{d}}\rangle - \langle\hat{\sigma}^z_{\boldsymbol{r}}\rangle\langle\hat{\sigma}^z_{\boldsymbol{r}+\boldsymbol{d}}\rangle$ has been measured for a mixture of two hyperfine states of fermionic ^{6}Li in a square optical lattice [20]. At half filling, long-range AF correlations extending throughout the lattice (size 10×10 sites) were observed at temperatures as low as $T/T_F \approx 0.06$, where $T_F = 4t/k_B$ is the Fermi temperature in the lattice.

Ultracold atom quantum simulators allow to directly control and tune the spin-imbalance (spin polarization) of the system, which in the case of the half-filled Fermi-Hubbard model induces canted antiferromagnetic correlations, as observed in [21] using ^{6}Li. Note that very large magnetic fields would be required for observing this effect in solid-state materials. Very recently, a bilayer Hubbard model was realized with ^{40}K, where tomographic imaging allowed to address both layers individually [65]. With increasing interlayer tunneling a crossover from a planar antiferromagnetic Mott insulator to a band insulator of interlayer spin-singlets was observed, confirming previous theoretical expectations. Also the attractive ($U < 0$) Fermi-Hubbard model has been realized with ^{6}Li, where quantum-gas microscopy of doublon density correlations, in combination with QMC simulations, made it possible to estimate the strength of s-wave pairing correlations [22]. Major progress has thus been made in quantum simulations of magnetism and superconductivity in Fermi-Hubbard systems, as first proposed in [17].

Cold atom quantum simulators also allow observing out-of-equilibrium particle- and spin-dynamics in real time. For example, using ^{87}Rb a one-dimensional two-component Bose-Hubbard model (see Eq. (7)) was realized, which for strong coupling maps onto an effective

ferromagnetic Heisenberg spin chain. In this system, propagation of magnons and of two-magnon bound states was observed by quantum-gas microscopy [23]. More recently, spin-charge deconfinement was observed in ^{6}Li Fermi-Hubbard chains, where after sudden removal of one particle the spin and charge excitations (spinons and holons) were found to propagate with different, interaction-dependent velocities [24]. Spin diffusion and spin conduction were measured in a 2d fermionic Mott insulator of ultracold ^{40}K, using quantum-gas microscopy [25], thus opening up the possibility to gain further insight into the interplay of charge and spin in strongly correlated fermion systems.

Recent progress with Rydberg-excited and Rydberg-dressed quantum gases allows engineering long-range interactions, both in quantum spin systems and in itinerant lattice models. Spinless fermions with next-neighbor interaction on an anisotropic square lattice, with hopping only in one direction, were realized with Rydberg-dressed ^{6}Li [13], and the effect of the next-neighbor interaction on the decay dynamics of initially prepared charge-density waves was investigated. Quantum simulations of extended Fermi-Hubbard models are thus within reach of current experiments. For itinerant bosons with Rydberg excitations in an optical lattice, an extended 2-component Bose-Hubbard model description is appropriate, which includes, in addition to Eq. (7), a long-range van der Waals interaction $H_{vdW} = (C_6/2)\sum_{i\neq j}\hat{n}_{i\uparrow}\hat{n}_{j\uparrow}/|\boldsymbol{i}-\boldsymbol{j}|^6$. Here the pseudospin states $\uparrow$ ($\downarrow$) denote the Rydberg state (ground state), respectively, $\boldsymbol{i}$ and $\boldsymbol{j}$ are the positions of lattice sites i, j and C_6 is the van der Waals coefficient. Coherent driving by a laser populates the Rydberg state, which leads (within the rotating wave approximation) to an additional Rabi term $H_R = (\Omega/2)\sum_i \left(a^\dagger_{i\uparrow}a_{i\downarrow} + a^\dagger_{i\downarrow}a_{i\uparrow}\right) - \Delta\hat{n}_{i\uparrow}$ with Rabi frequency Ω and detuning Δ. Bosonic DMFT simulations yield a rich phase diagram including a devil's staircase of crystalline phases which extends into the supersolid regime, where crystalline and condensate long-range order coexist [66], see Fig. 8.

Alternatively, optical microtraps can be arranged in arbitrary geometries and loaded with single atoms, which can be individually addressed and excited to a Rydberg state. In this way, the quantum many-body dynamics of Ising-type quantum-spin models has been investigated for systems with up to 51 qbits [67].

5 Topological (many-body) states of ultracold atoms

Topological states of matter provide a new paradigm beyond Landau's approach towards classifying phases of matter [68]. A prime example in two spatial dimensions is the integer quantum Hall effect. According to the TKNN formula [69] its quantized transverse conductivity is determined by a topological invariant, the Chern number $n = (1/2\pi)\sum_m \int d^2\boldsymbol{k}\, \Omega_m(\boldsymbol{k})$, where the summation is over all occupied bands. Here $\Omega_m = i\big(\langle\partial_{k_x}u_m(\boldsymbol{k})|\partial_{k_y}u_m(\boldsymbol{k})\rangle - \langle\partial_{k_y}u_m(\boldsymbol{k})|\partial_{k_x}u_m(\boldsymbol{k})\rangle\big)$ is the Berry curvature, and $|u_m(\boldsymbol{k})\rangle$ is the lattice-periodic part of the Bloch state with quasimomentum $\boldsymbol{k}$ in band m. Laughlin's argument [70] proves that in systems of finite width a quantized Hall conductivity $\sigma_{xy} = ne^2/h$ implies the existence of chiral edge states. As shown by Haldane, time-reversal symmetry breaking can induce a quantum Hall state even if no net magnetic flux is applied to the 2d system [71].

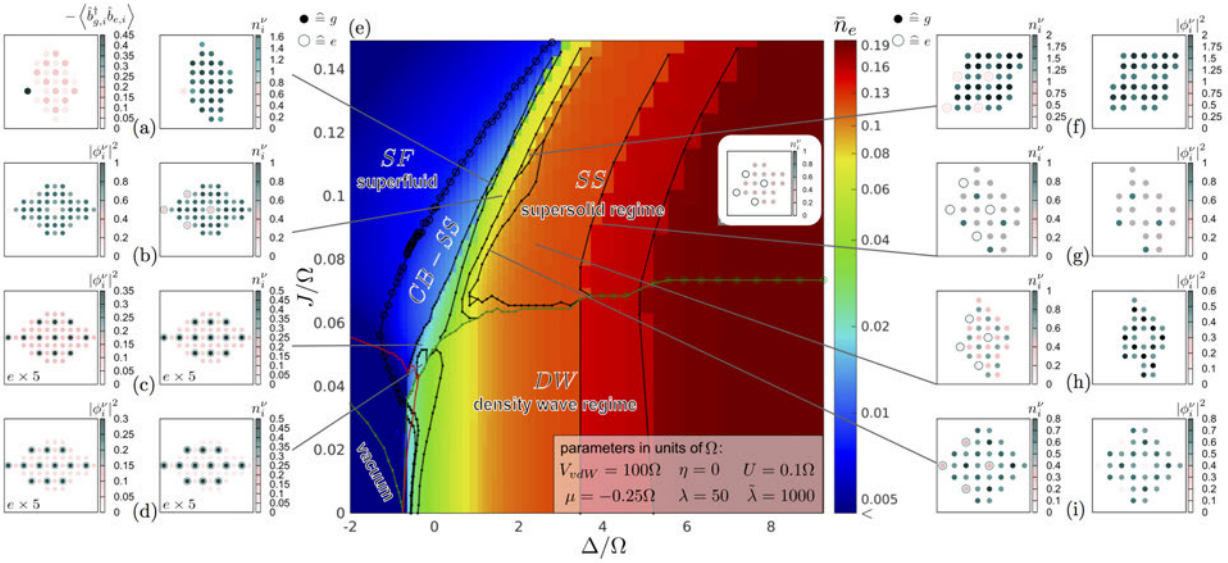

Fig. 8: *(e) Ground state phase diagram of a two-species extended bosonic Hubbard model with long-range (van der Waals) interaction of the excited Rydberg state, as a function of hopping amplitude (here denoted as J) and detuning Δ, in units of the Rabi frequency Ω. $\bar{n}_e$ is the lattice-averaged Rydberg fraction. The green (gray) line marks the emergence of a finite condensate order parameter. Black lines indicate transitions between different supersolid (SS) or density wave (DW) ordered phases, where circles denote second order and points first order. CB-SS indicates the checkerboard supersolid, and SF the homogeneous superfluid. Subfigures (a)-(d), (f)-(i) and the inset of (e) show the spatial distribution of different observables: density n_i^ν and condensate density $|\phi_i^\nu|^2$, where i is the lattice site index and $\nu = g(e)$ here denotes the ground (Rydberg excited) state. In addition, the correlation function $\langle b_{g,i}^\dagger b_{e,i} \rangle$, sensitive to checkerboard order, is shown, where $b^\dagger(b)$ denote the bosonic creation (annihilation) operators. Parameters given in the inset of (e) are: the ratio η of excited state hopping and ground state hopping, the van der Waals interaction strength $V_{vdW} = C_6/a^3$, and the onsite interaction ratios $\lambda = U_{\uparrow\downarrow}/U_\downarrow$ and $\tilde{\lambda} = U_\uparrow/U_\downarrow$, see Eq. (7), where we use the notation $\uparrow \hat{=} e$ and $\downarrow \hat{=} g$. Reprinted figure with permission from [66]. Copyright 2017 by the American Physical Society.*

More recently, time-reversal invariant topological insulators have been discovered, such as the quantum spin Hall (QSH) state, which is characterized by a Z_2 topological invariant and helical edge states inside the bulk band gap. An important model system featuring a QSH state is the Kane-Mele model [72], which consists of time-reversed copies of Haldane's model [71], discussed below. In solid-state systems quantum (spin-) Hall states can be detected by measuring band structures via angle-resolved photoemission or by measuring the Hall conductivity. But in these systems it is hard to measure the Berry curvature, or to study topological states of matter in the presence of tunable two-particle interactions.

Synthetic gauge fields, i.e., synthetic flux or spin-orbit coupling, have been realized in neutral ultracold atoms. Here we will focus on gauge fields in optical lattices achieved by time-periodic driving, in particular by laser-induced tunnelling [73–76] and in shaken lattices [77–79]. These techniques allow creating strong effective magnetic flux and topologically non-trivial states.

They are examples for Floquet engineering, which allows to design and tune band structures, interactions, quantum states and effective (Floquet-) Hamiltonians, by time-periodic driving [80]. Important model systems have already been realized in this way, in particular the Harper-Hofstadter (HH) [74, 75] and Haldane Hamiltonians [78].
The topological Haldane model [71] describes a quantum anomalous Hall state in the absence of a net flux and has the form

$$\hat{H} = -\sum_{\langle ij\rangle} t_{ij}\,\hat{a}_i^\dagger \hat{a}_j - \sum_{\langle\langle ij\rangle\rangle} t'_{ij}\,e^{i\phi_{ij}}\hat{a}_i^\dagger \hat{a}_j + \text{h.c.} + \Delta_{AB}\sum_{i\in A}\hat{a}_i^\dagger\hat{a}_i \tag{10}$$

where the indices $i(j)$ label the sites of a honeycomb lattice, t_{ij} and t'_{ij} are real hopping amplitudes between pairs of nearest neighbors $\langle ij\rangle$ and next-nearest neighbors $\langle\langle ij\rangle\rangle$, respectively, ϕ_{ij} is a phase, and Δ_{AB} is a staggered energy offset between the two sublattices A and B. The Haldane model has been realized experimentally [78] by "lattice shaking", i.e., by accelerated motion of a two-dimensional optical honeycomb lattice on an elliptical orbit $\boldsymbol{r}_{\text{lat}} = A\big(\cos(\omega t)\boldsymbol{e}_x + \cos(\omega t - \varphi)\boldsymbol{e}_y\big)$. The Berry curvature $\Omega_m(\boldsymbol{k})$ was measured semiclassically via the quasimomentum drift of a cloud of ultracold ^{40}K in the lowest band. More recently, a tomographic measurement of the full quasimomentum dependence of the Berry curvature of a tunable honeycomb lattice has been performed by monitoring the dynamics of the fermionic cloud after a sudden quench of the periodic driving [79].
The HH Hamiltonian describes a quantum particle on a tight-binding square lattice

$$\hat{H} = -\sum_{m,n} t\left(e^{i\phi_{mn}}\hat{a}^\dagger_{m+1,n}\hat{a}_{m,n} + \hat{a}^\dagger_{m,n+1}\hat{a}_{m,n}\right) + \text{h.c.}, \tag{11}$$

where the sites of the lattice are labeled by (m, n), in the presence of a strong magnetic flux, which is described by the Peierls phase ϕ_{mn}. It has been realized in optical lattices [74, 75], following the proposal [73], where the Peierls phase is imprinted by laser-assisted tunneling, as shown in the setup in Fig. 9. Due to a magnetic field gradient the energy offset Δ between neighboring sites in x-direction is much larger than the bare tunneling amplitude, suppressing hopping in this direction. Two additional laser beams with frequency difference $\omega = \omega_1 - \omega_2 = \Delta/\hbar$ and wave vector difference $\boldsymbol{q} = \boldsymbol{k}_1 - \boldsymbol{k}_2$ then induce resonant, laser-assisted tunneling in the x-direction. In the limit of high driving frequency ω this system can be described by an effective time-independent (Floquet-) Hamiltonian of the HH type as given in Eq. (11). The resulting Peierls phase is given by $\phi_{mn} = \boldsymbol{q}\cdot\boldsymbol{R}_{mn}$, where $\boldsymbol{R}_{mn}$ is the position of lattice site (m, n). One defines a dimensionless flux per plaquette of the lattice as $\alpha = \Phi/2\pi$, where Φ is the accumulated Peierls phase on a closed path around the plaquette. The Chern number of the lowest band of this system has been measured for $\alpha = 1/4$ in a modified, all-optical set-up [76]. Realizing a QSH state by filling the Chern bands with ultracold fermions and detecting the associated edge states remains an open challenge for experiments. Note, however, that edge states, and also a local Chern marker characterizing bulk topology, have been recently observed in setups where one spatial dimension is replaced by a "synthetic dimension" encoded in different internal (hyperfine) states, see for example [81].

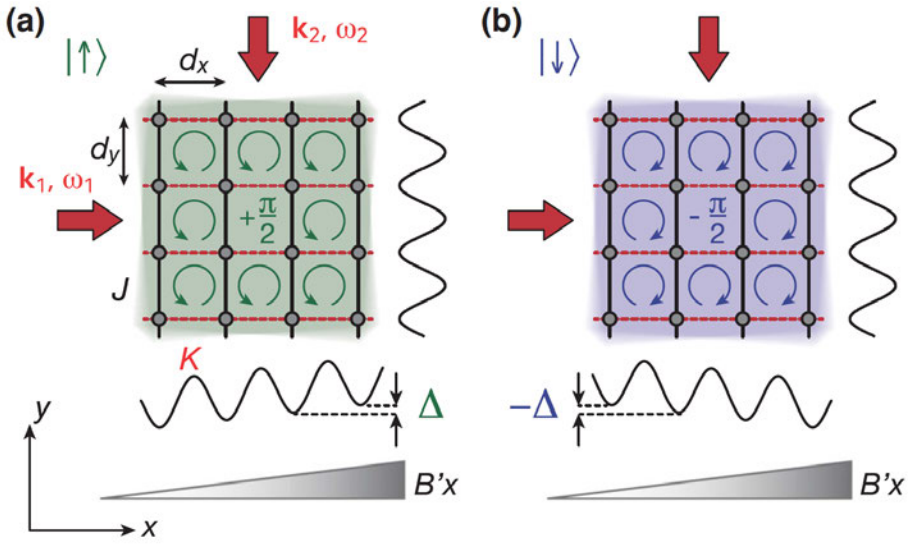

Fig. 9: *Experimental set-up for the realization of the Harper-Hofstadter Hamiltonian [74]. Two time-reversed copies of the HH-Hamiltonian (11) with opposite flux were realized for two hyperfine states labeled by* $|\uparrow\rangle, |\downarrow\rangle$. *Reprinted figure with permission from [74]. Copyright 2013 by the American Physical Society.*

Cold atoms with synthetic gauge fields are well suited for studying interacting topological many-body states. From a theoretical perspective, noninteracting topological insulators have been studied intensely and are quite well understood [68], but many open questions remain regarding the effect of two-particle interactions on topological bands. One promising approach [82] allows to extract (integer) topological invariants of interacting lattice systems from the zero-frequency Green's function alone, via an effective noninteracting "topological Hamiltonian" $h_{\rm top}(\boldsymbol{k}) = -G^{-1}(\boldsymbol{k}, i\omega{=}0)$. It can be conveniently combined with (real-space) DMFT and allows to calculate topological invariants for strongly correlated fermionic systems, e.g., for interacting QSH states in Hubbard-type lattice models. This approach has been applied to calculate the phase diagram of the time-reversal-symmetric fermionic Hofstadter-Hubbard model

$$\hat{H} = -t \sum_j \left(\hat{c}^\dagger_{j+\boldsymbol{e}_x} e^{i2\pi\gamma\sigma^x} \hat{c}_j + \hat{c}^\dagger_{j+\boldsymbol{e}_y} e^{i2\pi\alpha x\sigma^z} \hat{c}_j + \text{h.c.} \right) + \sum_j \left((-1)^x \lambda \hat{c}^\dagger_j \hat{c}_j + U \hat{n}_{i\uparrow} \hat{n}_{i\downarrow} \right) \quad (12)$$

with a staggered potential λ and additional spin-orbit coupling γ. Here $\boldsymbol{e}_x$, $\boldsymbol{e}_y$ are the primitive lattice vectors in x- and y-direction of a square lattice and $c^\dagger_j = (c^\dagger_{j\uparrow}, c^\dagger_{j\downarrow})$ denotes the creation operator at site $j = (x, y)$. An interaction-driven transition into the QSH state has been observed and the bulk-edge correspondence has been verified [83]. Moreover, the formation of a smooth topological interface in the bulk of the optical lattice has been proposed and studied theoretically by ramping up the staggered potential $\lambda(x)$ in the model (12) as a function of the x-coordinate [84], as shown in Fig. 10. By real-space DMFT simulations it was found that the gapless edge states at the interface are visible in an enhanced local compressibility. The latter can be directly related to non-local density-density correlations, which could in principle be measured by quantum-gas microscopy [19].

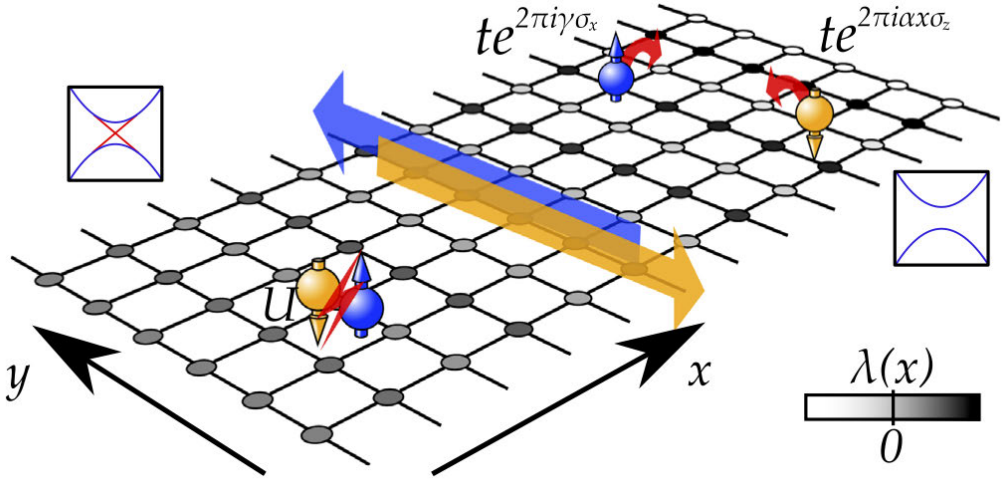

Fig. 10: *Topological Hofstadter interface: Schematic representation of the Hofstadter-Hubbard model, given by Eq. (12), in a cylinder geometry, with a staggered potential $\lambda(x)$ linearly increasing across the lattice in x-direction. Reprinted figure with permission from [84]. Copyright 2019 by the American Physical Society.*

The measurement of topological invariants in interacting quantum gases is challenging. In [85] it was shown for a spin-½ Haldane-Hubbard model that from the single-particle density-matrix (SPDM) of the system the effective topological Hamiltonian $h_{\rm top}(\boldsymbol{k})$ can be extracted, and thus the Chern number calculated and the topological phase transition determined. Furthermore, in this work a general experimental tomography scheme was proposed for measuring the SPDM of interacting fermions in bipartite lattices, based on a sudden quench of the system to a non-interacting lattice Hamiltonian, and subsequent time-of-flight measurement.

Topological band insulators are symmetry-protected topological (SPT) phases, with a bulk gap and nontrivial surface states which are protected by symmetry. Alternatively, a many-body system may have intrinsic topological order, with topological ground state degeneracy and fractional excitations [86]. Optical flux lattices may be a promising experimental platform for realizing fractional Chern insulators in ultracold atoms [87]. Topological order could be observed by measuring nonlocal correlation functions, for example string order, which has already been detected in a 1d bosonic Mott insulator [88].

6 Disorder and localization

Effects of disorder, such as localization or glassiness, are important in solid-state materials, where defects are intrinsically present and unavoidable. In particular, conducting properties of electronic systems are strongly affected by scattering from defects. In itinerant electronic systems metal-insulator transitions can occur which are driven by the interplay between spatial randomness and two-particle interactions. Noninteracting, disordered systems are rather well understood, see for example the review [89]. This is due to techniques such as the scaling theory of localization, which considers the dimensionless conductance $g \equiv G/(e^2/\hbar)$ and argues that

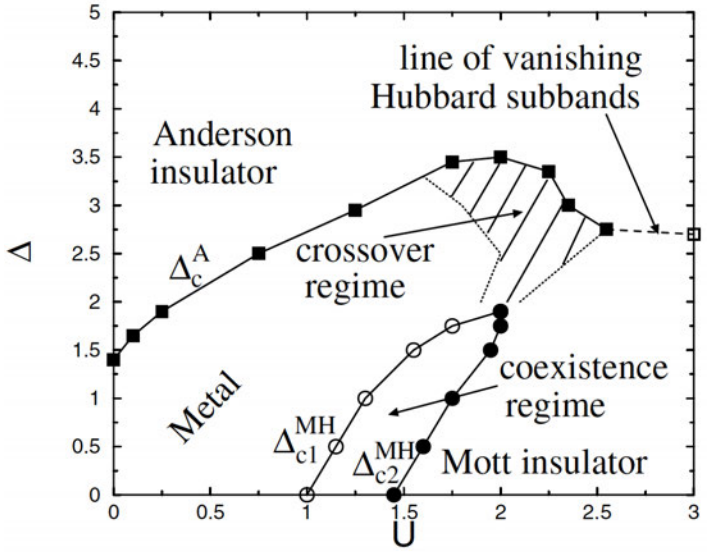

Fig. 11: *Paramagnetic ground state phase diagram of the fermionic Anderson-Hubbard model at half filling, determined by DMFT in combination with typical-medium theory. Reprinted figure with permission from [94]. Copyright 2005 by the American Physical Society.*

its dependence on the linear system size can be expressed as $\frac{d\ln g}{d\ln L} = \beta(g)$. In spatial dimensions $d = 1$ and 2 this leads in the thermodynamic limit $L \to \infty$ always to insulating behavior, corresponding to completely localized single-particle states, since $\beta(g) < 0$. On the other hand, in $d = 3$ one finds that $\beta(g_c) = 0$ at a critical value g_c of the conductance. This implies a mobility edge between (Anderson-)localized and extended single-particle states, and a metal-insulator transition as a function of disorder strength or chemical potential, as already predicted by Anderson in his seminar paper [90].

Ultracold atomic quantum simulations of relevant theoretical models offer high tunability of the type and strength of disorder, via quasi-periodic optical lattices or optical speckle potentials. In addition, two-particle interactions are tunable via Feshbach resonances, and also the (bosonic or fermionic) quantum statistics can be tuned by an appropriate choice of the atomic species. Moreover, non-equilibrium dynamics can be monitored in-situ in real time, which allows to probe many-body localization (MBL), as will be discussed below. We will, in the following, only consider quenched disorder potentials, corresponding to static, randomly placed defects which do not change on the experimental timescales.

Ultracold bosons have for the first time allowed direct observation in real space of an exponentially localized matter wave $\Psi_{\rm BEC}(x) \sim e^{-|x|/\xi}$, for example by imaging an expanding, non-interacting Bose-Einstein condensate in a 1d disordered optical Speckle potential [91]. Three-dimensional Anderson localization has been observed in ultracold fermionic ^{40}K, where an exponentially localized component of the cloud was detected, corresponding to particles below the mobility edge [92].

Major theoretical challenges remain in studies of quantum many-body systems with (strong) disorder and interaction. It has been predicted that two-particle interactions can lead to a metal-insulator transition in 2d disordered Fermi gases [93], in contrast to the non-interacting case.

Optical lattice quantum simulations are well suited for studying the interplay between strong local correlations, captured by the Hubbard model and leading e.g., to a Mott metal-insulator transition, and Anderson localization induced by strong disorder. Developments in DMFT have led to theoretical progress on this topic. The fermionic Anderson-Hubbard model is a disordered version of Eq. (1), where the onsite energies ε_i are independently sampled from a probability distribution $p(\varepsilon)$ of width Δ. Important disorder types are box disorder with a flat, bounded distribution $p(\varepsilon) = \Theta\big(\Delta/2-|\varepsilon|\big)/\Delta$, or optical Speckle disorder with $p(\varepsilon) = \Theta(\varepsilon)\exp(-\varepsilon/\Delta)/\Delta$, where $\Theta(x)$ is the Heaviside function. The fermionic Anderson-Hubbard model with box disorder has been studied at half filling by DMFT in combination with typical-medium theory (TMT) [94]. TMT is built on the concept that the typical (i.e. most probable) value of the local density of states (LDOS) $A_{i\sigma}(\omega) = -\frac{1}{\pi}\mathrm{Im}G_{ii\sigma}(\omega+i0^+)$ can be considered as a mean-field for the Anderson localization transition. In particular, the typical LDOS vanishes inside the Anderson insulator, in contrast to the average density of states. The resulting non-magnetic ground state phase diagram, see Fig. 11, clearly shows that weak interactions can induce delocalization in the Anderson insulator. This corresponds to re-entrant metallic behavior, which also occurs when disorder is added to the Mott insulator. Later DMFT studies also considered the experimentally realistic disorder distribution for optical Speckle potentials [95], and included the possibility of antiferromagnetic ordering, which leads to a novel antiferromagnetic metallic phase [96].

A quantum simulation of the fermionic Anderson-Hubbard model on a cubic optical lattice has been performed with ^{40}K, where disorder was induced by an additional optical Speckle potential [97]. A transport-type measurement of localization properties was performed where the center-of-mass velocity was detected after applying a magnetic field gradient. This velocity was found to decrease with increasing disorder, and to vanish at a critical disorder strength Δ_c, in agreement with an Anderson metal-insulator transition. Increasing the Hubbard interaction in the Anderson insulator led to delocalization, as shown in Fig. 12, which qualitatively confirms the DMFT prediction [94].

On the other hand, the disordered Bose-Hubbard model [31] describes effects of randomness in strongly correlated bosonic systems, for example in superfluid ^{4}He immersed in random pores of Vycor. It is given by Eq. (5) with onsite energies ε_i sampled from a probability distribution of width Δ. In the ground state, an insulating and compressible Bose glass (BG) phase has been predicted, in addition to the Mott insulator (MF) and the superfluid (SF) [31]. The properties of the BG have been the subject of numerous theoretical studies. In one spatial dimension, DMRG simulations have provided early insight [98], but less has been known in higher dimensions. Simple arithmetic averaging over disorder cannot describe the BG phase, since it effectively restores translational invariance. This has motivated development of a stochastic mean-field theory (SMFT), which maps the inhomogeneous system with spatial fluctuations of the condensate onto an ensemble of effective single-site problems, each coupled to a mean-field bath with condensate order parameter ψ, subject to a probability distribution $P(\psi)$ that is determined self-consistently [99, 100], as shown in Fig. 13 (left). In this way, the BG phase with its disorder-induced localization is captured, with a non-trivial dependence on spatial dimen-

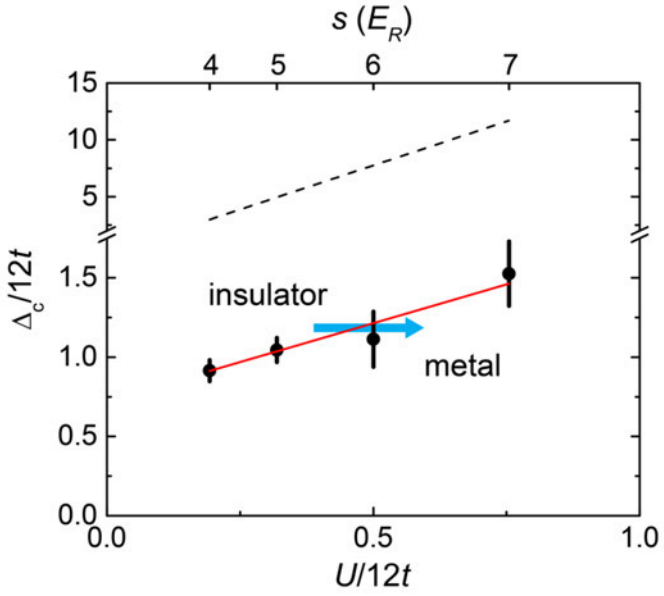

Fig. 12: *Critical disorder-strength of the disorder-driven fermionic metal-insulator transition measured for ultracold ^{40}K in a cubic lattice with Speckle disorder. Interaction-induced delocalization can be clearly seen. Reprinted figure with permission from [97]. Copyright 2015 by the American Physical Society.*

sion beyond mean-field scaling. The method can be applied to realistic disorder types such as optical Speckle potentials, and is formulated directly in the thermodynamic limit, thus avoiding finite-size effects. The MI, SF and BG phases are distinguished by their values of the average condensate order parameter ψ and the compressibility $\partial n/\partial \mu$. When including collective excitations of the BG in the SMFT calculation [100], one observes that the transition from MI to SF in the ground state of the disordered Bose-Hubbard model always occurs via an intermediate BG phase. This has been independently shown by QMC studies and a "theorem of inclusions" [101]. In the strongly interacting regime, at constant filling, increasing the disorder strength can lead to re-entrant superfluidity, i.e., drive the system from the insulator back into the superfluid phase. This was observed in SMFT calculations with a finite lattice coordination number $z = 6$ (see Fig. 13 (right)) [100] and in QMC simulations on a cubic lattice [101].

The disordered Bose-Hubbard model has been realized experimentally in a cubic optical lattice with an additional short-wavelength optical Speckle potential [102]. After switching on the Speckle potential, a strong reversible decrease of the condensate fraction was observed, which indicates that the interacting Bose-Einstein condensate is indeed localized by disorder. This was confirmed by measurement of mass transport in the lattice. Distinguishing the MI and BG phases would require additional measurements of the excitation spectrum or the compressibility, which were not performed in this experiment. Also, presumably due to finite temperature, no disorder-induced re-entrant superfluidity was observed.

Our discussion of localization transitions so far has focused on thermodynamic equilibrium and low temperatures. However, disordered and isolated quantum many-body systems may fail to thermalize, thus violating ergodicity, as was found in a perturbative study [103]. This so-called

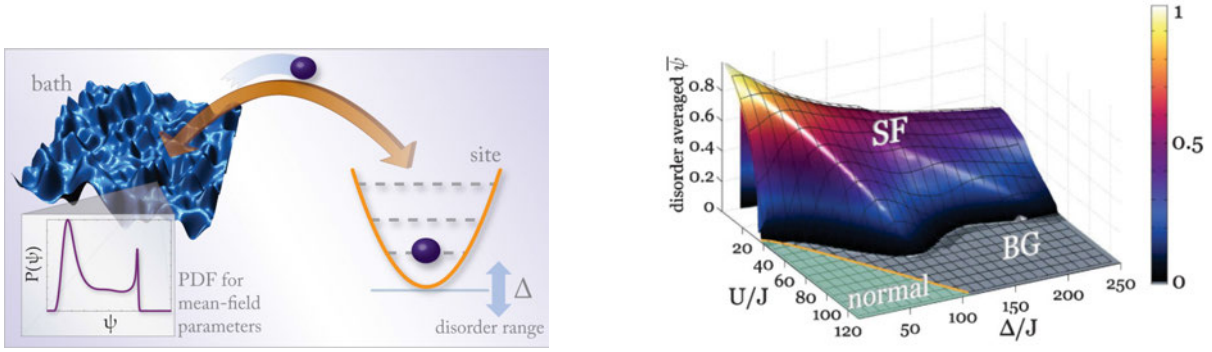

Fig. 13: *(left) Schematic illustration of SMFT. The lattice model is mapped onto an ensemble of effective single-site problems, each of which is coupled to a condensate mean-field bath. Spatially random fluctuations are captured by a statistical distribution of the condensate order parameter ψ. Reprinted figure with permission from [99]. (right) Phase diagram of the Bose-Hubbard model with lattice coordination number $z = 6$ and box disorder at filling $n = 1$ and $T = 0.03U$ (J denotes the hopping). At the protruding Mott lobe re-entrant superfluidity occurs, i.e., increasing the disorder strength drives a series of SF-insulator transitions. Reprinted figure with permission from [100]. Copyright 2010 by the American Physical Society.*

many-body localization (MBL) has since been the subject of numerous theoretical studies using different numerical and analytical approaches; for a review see [104]. Remarkably, a many-body localized system can remain fully insulating even at $T > 0$, different from an interacting Anderson insulator, which is only strictly insulating at $T = 0$. In the out-of equilibrium real-time dynamics of MBL systems, when initialized in a non-entangled state, entanglement spreads logarithmically, in contrast to thermal states or noninteracting Anderson insulators [104]. For a 1d quantum spin chain with short-range interactions a quasi-rigorous proof for the existence of MBL has been given [105]. Much less is known in $d > 1$, due to a lack of exact analytical solutions or reliable numerical simulation of quantum many-body dynamics. There have been arguments that MBL may be absent in $d > 1$ [106] and even MBL in disordered, interacting quantum spin chains has recently been challenged [107].

Quantum simulations with ultracold atoms have provided new insight into MBL. For fermions in a 1d incommensurate optical superlattice, described by the Aubry-André model which contains quasi-random disorder, it was observed that an initially prepared particle-density wave state does not decay in time, provided randomness is sufficiently strong [108]. This indicates a breakdown of thermalization. In a later measurement the real-time dynamics of a bosonic ^{87}Rb ensemble in a 2d disordered optical lattice after a quantum quench was observed. It was found that an initially prepared density domain wall fails to decay completely if the disorder strength is above a critical value, leading to a non-thermalized (quasi-) steady state [109]. The spatial decay length of the density distribution in the steady state was found to diverge at the critical disorder strength, i.e., at the (possible) MBL transition observed here. However, it remains to be seen whether the MBL phenomena observed on the time scales accessible in these experiments represent a stable localized quantum phase, or whether they correspond to a metastable transient regime that emerges before thermalization sets in at much longer time scales [104].

7 Outlook

Analog quantum simulations of Hubbard-type models with ultracold atoms in optical lattices have already been very successful. One future goal will be to achieve even lower temperature (entropy) in optical lattices, in order to reach exotic low-temperature phases such as d-wave superfluidity in the Fermi-Hubbard model [17]. Hybrid quantum simulators with degenerate fermionic clouds coupled to phonons of trapped ion crystals can provide insight into the effect of additional electron-phonon coupling in strongly correlated systems [14].
Tunable long-range interactions in ultracold atomic ensembles will lead to novel physics compared to strongly correlated electronic systems. They can be induced by different approaches, including Rydberg excitations, heteronuclear molecules, magnetic dipolar moments, and coupling of quantum gases to single- or few-mode optical cavities. In this way, for example, supersolid phases have already been realized [110, 111].
Fermionic alkaline-earth-like elements (for example ^{173}Yb or ^{87}Sr) with their large nuclear spin decoupled from electronic angular momentum have emerged as platforms for simulating itinerant lattice models with orbital degeneracy or higher internal symmetries, which could allow quantum simulation of more exotic states of matter [112, 7, 8].
Due to the unprecedented local access in preparation and measurement of quantum states that is provided by optical quantum-gas microscopy, optical lattice quantum simulators are also ideally suited to study far-from-equilibrium quantum many-body dynamics. Fundamental open questions that will be further investigated in this way range from many-body-localization to quantum chaos.

Acknowledgments

Support by the Deutsche Forschungsgemeinschaft via DFG SPP 1929 GiRyd and under Project No. 277974659 via Research Unit FOR 2414 is gratefully acknowledged.

References

[1] I. Bloch, J. Dalibard, and W. Zwerger, Rev. Mod. Phys. **80**, 885 (2008)

[2] W. Hofstetter and T. Qin, J. Phys. B: At. Mol. Opt. Phys. **51**, 082001 (2018)

[3] R.P. Feynman, Int. J. Theor. Phys. **21**, 467 (1982)

[4] P.A. Lee, N. Nagaosa, and X.-G. Wen, Rev. Mod. Phys. **78**, 17 (2006)

[5] K. Le Hur and T.M. Rice, Ann. Phys. **324**, 1452 (2009)

[6] M. Greiner, O. Mandel, T. Esslinger, T.W. Hänsch, and I. Bloch, Nature **415**, 39 (2002)

[7] C. Honerkamp and W. Hofstetter, Phys. Rev. Lett. **92**, 170403 (2004)

[8] A. Rapp, G. Zarand, C. Honerkamp, and W. Hofstetter, Phys. Rev. Lett. **98**, 160405 (2007)

[9] M. Troyer and U.-J. Wiese, Phys. Rev. Lett. **94**, 170201 (2005)

[10] G. Cohen, E. Gull, D.R. Reichman, and A.J. Millis, Phys. Rev. Lett. **115**, 266802 (2015)

[11] I.M. Georgescu, S. Ashhab, and F. Nori, Rev. Mod. Phys. **86**, 153 (2014)

[12] J. Hubbard, Proc. R. Soc. Lond. A **276**, 238 (1963)

[13] E. Guardado-Sanchez, B.M. Spar, P. Schauss, R. Belyansky, J.T. Young, P. Bienias, A.V. Gorshkov, T. Iadecola, W.S. Bakr, Phys. Rev. X **11**, 021036 (2021)

[14] U. Bissbort, D. Cocks, A. Negretti, Z. Idziaszek, T. Calarco, F. Schmidt-Kaler, W. Hofstetter, R. Gerritsma, Phys. Rev. Lett. **111**, 080501 (2013)

[15] A. Georges, G. Kotliar, W. Krauth, and M.J. Rozenberg, Rev. Mod. Phys. **68**, 13 (1996)

[16] P.W. Anderson, Science **235**, 1196 (1987)

[17] W. Hofstetter, J.I. Cirac, P. Zoller, E. Demler, and M.D. Lukin, Phys. Rev. Lett. **89**, 220407 (2002)

[18] D. Jaksch, C. Bruder, J.I. Cirac, C.W. Gardiner, and P. Zoller, Phys. Rev. Lett. **81**, 3108 (1998)

[19] W.S. Bakr, A. Peng, M.E. Tai, R. Ma, J. Simon, J.I. Gillen, S. Fölling, L. Pollet, and M. Greiner, Science **329**, 547 (2010); J.F. Sherson, C. Weitenberg, M. Endres, M. Cheneau, I. Bloch, and S. Kuhr, Nature **467**, 68 (2010)

[20] A. Mazurenko, C.S. Chiu, G. Ji, M.F. Parsons, M. Kanasz-Nagy, R. Schmidt, F. Grusdt, E. Demler, D. Greif and M. Greiner, Nature **545**, 462 (2017)

[21] P.T. Brown, D. Mitra, E. Guardado-Sanchez, P. Schauß, S.S. Kondov, E. Khatami, T. Paiva, N. Trivedi, D.A. Huse, W.S. Bakr, Science **357**, 1385 (2017)

[22] D. Mitra, P.T. Brown, E. Guardado-Sanchez, S.S. Kondov, T. Devakul, D.A. Huse, P. Schauß and W.S. Bakr, Nat. Phys. **14**, 173 (2018)

[23] T. Fukuhara, P. Schauß, M. Endres, S. Hild, M. Cheneau, I. Bloch and C. Gross, Nature **502**, 76 (2013)

[24] J. Vijayan, P. Sompet, G. Salomon, J. Koepsell, S. Hirthe, A. Bohrdt, F. Grusdt, I. Bloch, and C. Gross, Science **367**, 186 (2020)

[25] M.A. Nichols, L.W. Cheuk, M. Okan, T.R. Hartke, E. Mendez, T. Senthil, E. Khatami, H. Zhang, and M.W. Zwierlein, Science **363**, 383 (2019)

[26] R. Grimm, M. Weidemüller and Y.B. Ovchinnikov, Adv. At. Mol. Opt. Phys. **42**, 95 (2000)

[27] J. Struck, C. Ölschläger, R. Le Targat, P. Soltan-Panahi, A. Eckardt, M. Lewenstein, P. Windpassinger, and K. Sengstock, Science **333**, 996 (2011)

[28] G.-B. Jo, J. Guzman, C.K. Thomas, P. Hosur, A. Vishwanath, and D.M. Stamper-Kurn, Phys. Rev. Lett. **108**, 045305 (2012)

[29] T. Uehlinger, G. Jotzu, M. Messer, D. Greif, W. Hofstetter, U. Bissbort, and T. Esslinger, Phys. Rev. Lett. **111**, 185307 (2013)

[30] U. Bissbort: *Dynamical effects and disorder in ultracold bosonic matter*, PhD Thesis, Johann Wolfgang Goethe-Universität, Frankfurt am Main (2013)

[31] M.P.A. Fisher, P.B. Weichman, G. Grinstein, and D.S. Fisher, Phys. Rev. B **40**, 546 (1989)

[32] S. Will, T. Best, U. Schneider, L. Hackermüller, D.-S. Lühmann, and I. Bloch, Nature **465**, 197 (2010)

[33] U. Bissbort, F. Deuretzbacher, and W. Hofstetter, Phys. Rev. A **86**, 023617 (2012)

[34] M. Köhl, H. Moritz, T. Stöferle, K. Günter, and T. Esslinger, Phys. Rev. Lett. **94**, 080403 (2005)

[35] E. Altman, E. Demler, and M.D. Lukin, Phys. Rev. A **70**, 013603 (2004)

[36] J. Simon, W.S. Bakr, R. Ma, M.E. Tai, P.M. Preiss, and M. Greiner, Nature **472**, 307 (2011)

[37] C.A. Regal and D.S. Jin, Phys. Rev. Lett. **90**, 230404 (2003); S. Gupta, Z. Hadzibabic, M.W. Zwierlein, C.A. Stan, K. Dieckmann, C.H. Schunck, E.G.M. van Kempen, B.J. Verhaar, and W. Ketterle, Science **300**, 1723 (2003)

[38] A. Schirotzek, Y.-il Shin, C.H. Schunck, and W. Ketterle,
Phys. Rev. Lett. **101**, 140403 (2008)

[39] J.T. Stewart, J.P. Gaebler, and D.S. Jin, Nature **454**, 744 (2008)

[40] U. Bissbort, S. Götze, Y. Li, J. Heinze, J.S. Krauser, M. Weinberg, C. Becker,
K. Sengstock, and W. Hofstetter, Phys. Rev. Lett. **106**, 205303 (2011)

[41] R. Jördens, N. Strohmaier, K. Günter, H. Moritz, and T. Esslinger,
Nature **455**, 204 (2008)

[42] C. Weitenberg, M. Endres, J.F. Sherson, M. Cheneau, P. Schauß, T. Fukuhara, I. Bloch
and S. Kuhr, Nature **471**, 319 (2011)

[43] D. Greif, M.F. Parsons, A. Mazurenko, C.S. Chiu, S. Blatt, F. Huber, G. Ji,
and M. Greiner, Science **351**, 953 (2016)

[44] M. Snoek, I. Titvinidze, C. Toke, K. Byczuk, and W. Hofstetter,
New J. Phys. **10**, 093008 (2008)

[45] E. Gull, A.J. Millis, A. Lichtenstein, A.N. Rubtsov, M. Troyer, and P. Werner,
Rev. Mod. Phys. **83**, 349 (2011)

[46] E.V. Gorelik, I. Titvinidze, W. Hofstetter, M. Snoek, and N. Blümer,
Phys. Rev. Lett. **105**, 065301 (2010)

[47] G. Kotliar and D. Vollhardt, Phys. Today **57**, 53 (2004)

[48] K. Byczuk and D. Vollhardt, Phys. Rev. B **77**, 235106 (2008); A. Hubener, M. Snoek,
and W. Hofstetter, Phys. Rev. B **80**, 245109 (2009)

[49] N. Prokof'ev and B. Svistunov, Phys. Rev. Lett. **92**, 15703 (2004)

[50] S. Trotzky, L. Pollet, F. Gerbier, U. Schnorrberger, I. Bloch, N. Prokof'ev, B. Svistunov,
and M. Troyer, Nat. Phys. **6**, 998 (2010)

[51] U. Schneider, L. Hackermüller, S. Will, Th. Best, I. Bloch, T.A. Costi, R.W. Helmes,
D. Rasch, and A. Rosch, Science **322**, 1520 (2008)

[52] S. Taie, R. Yamazaki, S. Sugawa, and Y. Takahashi, Nat. Phys. **8**, 825 (2012)

[53] E. Altman, W. Hofstetter, E. Demler, and M.D. Lukin, New J. Phys. **5**, 113 (2003)

[54] A. Sotnikov, D. Cocks, and W. Hofstetter, Phys. Rev. Lett. **109**, 065301 (2012)

[55] Y. Li, R. Bakhtiari, L. He, and W. Hofstetter, Phys. Rev. B **84**, 144411 (2011)

[56] Y. Li, M.R. Bakhtiari, L. He, and W. Hofstetter, Phys. Rev. A **85**, 023624 (2012)

[57] S. Fuchs, E. Gull, L. Pollet, E. Burovski, E. Kozik, T. Pruschke, and M. Troyer, Phys. Rev. Lett. **106**, 030401 (2011)

[58] R.A. Hart, P.M. Duarte, T.-L. Yang, X. Liu, T. Paiva, E. Khatami, R.T. Scalettar, N. Trivedi, D.A. Huse, and R.G. Hulet, Nature **519**, 211 (2015)

[59] A. Sotnikov and W. Hofstetter, Phys. Rev. A **89**, 063601 (2014); M. Hafez-Torbati and W. Hofstetter, Phys. Rev. B **100**, 035133 (2019)

[60] L. Bonnes, K.R.A. Hazzard, S.R. Manmana, A.M. Rey, and S. Wessel, Phys. Rev. Lett. **109**, 205305 (2012)

[61] S. Trotzky, P. Cheinet, S. Fölling, M. Feld, U. Schnorrberger, A.M. Rey, A. Polkovnikov, E.A. Demler, M.D. Lukin, and I. Bloch, Science **319**, 295 (2008)

[62] D.C. McKay and B. DeMarco, Rep. Prog. Phys. **74**, 054401 (2011)

[63] P. Medley, D.M. Weld, H. Miyake, D.E. Pritchard, and W. Ketterle, Phys. Rev. Lett. **106**, 195301 (2011)

[64] D. Greif, T. Uehlinger, G. Jotzu, L. Tarruell, and T. Esslinger, Science **340**, 1307 (2013)

[65] M. Gall, N. Wurz, J. Samland, C.F. Chan, and M. Köhl, Nature **589**, 40 (2021)

[66] A. Geißler, I. Vasić, and W. Hofstetter, Phys. Rev. A **95**, 063608 (2017)

[67] H. Bernien, S. Schwartz, A. Keesling, H. Levine, A. Omran, H. Pichler, S. Choi, A.S. Zibrov, M. Endres, M. Greiner, V. Vuletic, and M.D. Lukin, Nature **551**, 579 (2017)

[68] M.Z. Hasan and C.L. Kane, Rev. Mod. Phys. **82**, 3045 (2010)

[69] D.J. Thouless, M. Kohmoto, M.P. Nightingale, and M. den Nijs, Phys. Rev. Lett. **49**, 405 (1982)

[70] R.B. Laughlin, Phys. Rev. B **23**, 5632 (1981)

[71] F.D.M. Haldane, Phys. Rev. Lett. **61**, 2015 (1988)

[72] C.L. Kane and E.J. Mele, Phys. Rev. Lett. **95**, 226801 (2005)

[73] D. Jaksch and P. Zoller, New J. Phys. **5**, 56 (2003)

[74] M. Aidelsburger, M. Atala, M. Lohse, J.T. Barreiro, B. Paredes, and I. Bloch, Phys. Rev. Lett. **111**, 185301 (2013)

[75] H. Miyake, G.A. Siviloglou, C.J. Kennedy, W.C. Burton, and W. Ketterle, Phys. Rev. Lett. **111**, 185302 (2013)

[76] M. Aidelsburger, M. Lohse, C. Schweizer, M. Atala, J.T. Barreiro, S. Nascimbene, N.R. Cooper, I. Bloch, and N. Goldman, Nat. Phys. **11**, 162 (2015)

[77] J. Struck, M. Weinberg, C. Ölschläger, P. Windpassinger, J. Simonet, K. Sengstock, R. Höppner, P. Hauke, A. Eckardt, M. Lewenstein, and L. Mathey, Nat. Phys. **9**, 738 (2013)

[78] G. Jotzu, M. Messer, R. Desbuquois, M. Lebrat, T. Uehlinger, D. Greif, and T. Esslinger, Nature **515**, 237 (2014)

[79] N. Fläschner, B.S. Rem, M. Tarnowski, D. Vogel, D.-S. Lühmann, K. Sengstock, and C. Weitenberg, Science **352**, 1091 (2016)

[80] A. Eckardt, Rev. Mod. Phys. **89**, 011004 (2017)

[81] T. Chalopin, T. Satoor, A. Evrard, V. Makhalov, J. Dalibard, R. Lopes, and S. Nascimbene, Nat. Phys. **16**, 1017 (2020)

[82] Z. Wang and S.-C. Zhang, Phys. Rev. X **2**, 031008 (2012)

[83] D. Cocks, P.P. Orth, S. Rachel, M. Buchhold, K. Le Hur, and W. Hofstetter, Phys. Rev. Lett. **109**, 205303 (2012);
P. Kumar, T. Mertz, and W. Hofstetter. Phys. Rev. B **94**, 115161 (2016)

[84] B. Irsigler, J.-H. Zheng, and W. Hofstetter, Phys. Rev. Lett. **122**, 010406 (2019)

[85] J.-H. Zheng, B. Irsigler, L. Jiang, C. Weitenberg, and W. Hofstetter, Phys. Rev. A **101**, 013631 (2020)

[86] T. Senthil, Annu. Rev. Condens. Matter Phys. **6**, 299 (2015)

[87] N.R. Cooper and J. Dalibard, Phys. Rev. Lett. **110**, 185301 (2013)

[88] M. Endres, M. Cheneau, T. Fukuhara, C. Weitenberg, P. Schauss, C. Gross, L. Mazza, M.C. Banuls, L. Pollet, I. Bloch, and S. Kuhr, Science **334**, 200 (2011)

[89] P.A. Lee and T.V. Ramakrishnan, Rev. Mod. Phys. **57**, 287 (1985)

[90] P.W. Anderson, Phys. Rev. **109**, 1492 (1958)

[91] J. Billy, V. Josse, Z. Zuo, A. Bernard, B. Hambrecht, P. Lugan, D. Clement, L. Sanchez-Palencia, P. Bouyer, and A. Aspect, Nature **453**, 891 (2008)

[92] S.S. Kondov, W.R. McGehee, J.J. Zirbel, and B. DeMarco, Science **334**, 66 (2011)

[93] S.V. Kravchenko and M.P. Sarachik, Rep. Prog. Phys. **67**, 1 (2003)

[94] K. Byczuk, W. Hofstetter, and D. Vollhardt, Phys. Rev. Lett. **94**, 056404 (2005)

[95] D. Semmler, J. Wernsdorfer, U. Bissbort, K. Byczuk, and W. Hofstetter, Phys. Rev. B **82**, 235115 (2010)

[96] K. Byczuk, W. Hofstetter, and D. Vollhardt, Phys. Rev. Lett. **102**, 146403 (2009)

[97] S.S. Kondov, W.R. McGehee, W. Xu, and B. DeMarco, Phys. Rev. Lett. **114**, 083002 (2015)

[98] S. Rapsch, U. Schollwöck, and W. Zwerger, Europhys. Lett. **46**, 559 (1999)

[99] U. Bissbort and W. Hofstetter, EPL **86**, 50007 (2009)

[100] U. Bissbort, R. Thomale, and W. Hofstetter, Phys. Rev. A **81**, 063643 (2010)

[101] V. Gurarie, L. Pollet, N.V. Prokof'ev, B.V. Svistunov, and M. Troyer, Phys. Rev. B **80**, 214519 (2009)

[102] M. White, M. Pasienski, D. McKay, S.Q. Zhou, D. Ceperley, and B. DeMarco, Phys. Rev. Lett. **102**, 055301 (2009);
M. Pasienski, D. McKay, M. White, and B. DeMarco, Nat. Phys. **6**, 677 (2010)

[103] D.M. Basko, I.L. Aleiner, and B.L. Altshuler, Ann. Phys. **321**, 1126 (2006)

[104] R. Nandkishore and D.A. Huse, Annu. Rev. Condens. Matter Phys. **6**, 15 (2015)

[105] J.Z. Imbrie, Phys. Rev. Lett. **117**, 027201 (2016)

[106] W. De Roeck and F. Huveneers, Phys. Rev. B **95**, 155129 (2017)

[107] J. Suntajs, J. Bonca, T. Prosen, and L. Vidmar, Phys. Rev. E **102**, 062144 (2020)

[108] M. Schreiber, S.S. Hodgman, P. Bordia, H.P. Lüschen, M.H. Fischer, R. Vosk, E. Altman, U. Schneider, and I. Bloch, Science **349**, 842 (2015)

[109] J.-y. Choi, S. Hild, J. Zeiher, P. Schauß, A. Rubio-Abadal, T. Yefsah, V. Khemani, D.A. Huse, I. Bloch, and C. Gross, Science **352**, 1547 (2016)

[110] F. Böttcher, J. Schmidt, M. Wenzel, J. Hertkorn, M. Guo, T. Langen, and T. Pfau, Phys. Rev. X **9**, 011051 (2019);
L. Tanzi, E. Lucioni, F. Fama, J. Catani, A. Fioretti, C. Gabbanini, R.N. Bisset, L. Santos, and G. Modugno, Phys. Rev. Lett. **122**, 130405 (2019);
L. Chomaz, D. Petter, P. Ilzhöfer, G. Natale, A. Trautmann, C. Politi, G. Durastante, R.M.W. van Bijnen, A. Patscheider, M. Sohmen, M.J. Mark, and F. Ferlaino, Phys. Rev. X **9**, 021012 (2019)

[111] J. Léonard, A. Morales, P. Zupancic, T. Esslinger and T. Donner, Nature **543**, 87 (2017)

[112] A.V. Gorshkov, M. Hermele, V. Gurarie, C. Xu, P.S. Julienne, J. Ye, P. Zoller, E. Demler, M.D. Lukin, and A.M. Rey, Nat. Phys. **6**, 289 (2010)